PCCP

PAPER

View Article Online
View Journal | View Issue

Cite this: *Phys. Chem. Chem. Phys.*, 2014, **16**, 26528

Illuminating surface atoms in nanoclusters by differential X-ray absorption spectroscopy†

Charles S. Spanjers,[a] Thomas P. Senftle,[a] Adri C. T. van Duin,[b] Michael J. Janik,[a] Anatoly I. Frenkel*[c] and Robert M. Rioux*[a]

Received 16th May 2014,
Accepted 15th July 2014

DOI: 10.1039/c4cp02146k

www.rsc.org/pccp

We use differential extended X-ray absorption fine structure (Δ-EXAFS) to monitor the Ar-induced surface restructuring of silica-supported Pd nanoclusters (1 nm diameter) at 77 K. Δ-EXAFS analysis shows 9 ± 2 nearest-neighbor Pd–Pd bonds expand by 0.104 ± 0.005 Å as a result of Ar adsorption. Atomistic molecular dynamics simulations provide evidence for a model in which Ar drives restructuring of under-coordinated Pd atoms, leading to an increased Pd–Pd bond length of surface Pd atoms with no change in overall nearest-neighbor Pd–Pd coordination number. Based on observations from the atomistic simulations, it is likely that under-coordinated atoms are trapped in metastable states at 77 K and Ar provides the kinetic energy needed to overcome the barrier for surface restructuring. Together, experiment and theory highlight the ability of Δ-EXAFS to probe surface atoms of Pd nanoclusters.

Introduction

Nanoscience relies on the ability of researchers to detect ultra-small changes on the atomic scale that arise from the non-bulk-like properties of nanostructures. Applications of such materials are far reaching—extending from drug delivery[1] to catalysis,[2] photonics,[3] magnetic storage,[4] and spintronics.[5] In catalysis, surface atoms of metal nanoparticles (under-coordinated surface atoms in particular) often control catalytic properties.[6–10] Detecting the number and coordination environment of surface metal atoms, as well as their response to stimuli (*i.e.* molecules), is of utmost importance in understanding catalytic behavior. X-ray absorption spectroscopy (XAS) is particularly well-suited for this task due to its sensitivity to local structure (within a few coordination shells around an X-ray absorbing atom) and its ability to be used *in situ*, but the inherent ensemble-averaging nature of XAS measurements that probe both interior (bulk) and surface atom types makes surface characterization difficult. External stimulation, such as the chemisorption of molecules, can be used to enhance the detectability of the surface atoms by XAS. For example, XAS can be used to determine the surface compositions of Pd and Pt in bimetallic nanoparticles by detecting changes in the X-ray absorption near edge structure (XANES) after CO adsorption.[11] The use of differential extended X-ray absorption fine structure (Δ-EXAFS) allows for more sensitive detection of local structure compared to traditional EXAFS. Applied to catalysis, this technique can isolate active surface atoms from spectator bulk atoms.[12–17] Application of this technique to magnetostriction makes detection of femtometer atomic displacements possible.[18]

Despite the number of methods developed in the last decade, improving the selectivity of structural probes to surface metal atoms in nm-scale nanoclusters remains one of the primary objectives of catalysis science. In this work we will show the application of a Δ-EXAFS method that we developed for probing surface atoms of SiO_2-supported Pd nanoclusters. The Δ-EXAFS data were obtained by measuring the EXAFS signals before and after Ar adsorption, and subsequently modeled by taking into account only the unsubtracted (surface) Pd contributions. In addition to EXAFS data analysis and modeling, we have also employed atomistic molecular dynamics (MD) simulations to differentiate between models compared in the EXAFS data analysis process, thus determining the most plausible mechanism for restructuring. Further application of the technique is not limited to a particular set of materials; instead, it can be applied to any system in which modulation causes small changes in local structure.

Experimental and computational methods

Synthesis of Pd/SiO_2

A 3% Pd/SiO_2 sample was synthesized using the strong electrostatic adsorption (SEA) method, according to a previously

[a] *Department of Chemical Engineering, Pennsylvania State University, University Park, Pennsylvania 16802, USA. E-mail: rioux@engr.psu.edu*
[b] *Department of Mechanical and Nuclear Engineering, Pennsylvania State University, University Park, Pennsylvania 16802, USA*
[c] *Physics Department, Yeshiva University, 245 Lexington Avenue, New York, New York 10016, USA. E-mail: anatoly.frenkel@yu.edu*

† Electronic supplementary information (ESI) available. See DOI: 10.1039/c4cp02146k

reported procedure.[19] $Pd(NH_3)_4(NO_3)_2$ was added to a slurry of silica (Davisil A60) at pH = 11. The sample was filtered, washed, and dried at 398 K prior to reduction at 438 K under flowing 4% H_2/He for 1 h.

X-ray absorption spectroscopy (XAS)

XAS measurements were performed at beamline 10-BM of the Advanced Photon Source (APS) at Argonne National Lab (ANL). The 3% Pd/SiO_2 catalyst ($\sim$50 mg) was pressed into a 4 mm ID cylindrical steel holder to obtain an edge step of $\sim$0.4 at the Pd K-edge. The sample was loaded into a specially designed *in situ* reactor cell (Fig. S1 in the ESI†) capable of heating the catalyst sample to 523 K for reduction and cooling to 77 K during XAS measurements. After loading the sample, the sample chamber was evacuated with a mechanical vacuum pump to a base pressure of 30 mTorr and subsequently pressure checked to ensure all fittings were installed correctly and the system had no leaks. Ultra-high purity (UHP, 99.999%) 3% H_2/He without further purification was used for reduction of the catalyst. All UHP grade gases were purchased from Praxair/GTS Welco. The concentrations of the analyzed impurities in UHP He were O_2 (<1 ppm), H_2O (<2 ppm), total hydrocarbons (THC, <0.5 ppm), and N_2 (<5 ppm). The UHP Ar contained O_2 (<1 ppm), H_2O (<3 ppm), total hydrocarbons (THC, <0.5 ppm), and N_2 (<4 ppm). UHP He and UHP Ar were passed through triple gas purifiers (Restek Super Clean gas purifier) to remove oxygen, moisture, and hydrocarbons to a purity of 99.9999% prior to admission onto the catalyst sample. The sample was purged at room temperature under flowing 3% H_2/He at a rate of 30 mL min^{-1} for 15 min before heating to 523 K and holding for 1 h. The system was purged with He at a rate of 30 mL min^{-1} for 20 min prior to cooling to remove absorbed and adsorbed hydrogen from the Pd nanoclusters (NCs). The sample was then immediately cooled to 77 K by sliding the sample holder into the liquid nitrogen Dewar with a magnet. The temperature of the catalyst was measured in a separate experiment to be 79 K. However, it is unclear if the thermocouple was inducing a heat loss and the cause of the increased temperature. Therefore, the temperature of the EXAFS measurements is assumed to be 77 K. All EXAFS scans were acquired in transmission geometry with an energy range from 200 eV before to 1227 eV after the Pd K-edge (24 350 eV). A reference Pd foil was placed between the transmission and reference ionization chambers for energy calibration and alignment. The EXAFS scans referred to as ''Clean Pd NCs'' were acquired under flowing He at a rate of 30 mL min^{-1} at 77 K. The EXAFS scans referred to as ''After Ar adsorption'' were acquired under a mixture of Ar (5 mL min^{-1}) and He (30 mL min^{-1}) at 77 K. At this partial pressure of Ar ($\sim$100 Torr), we expect both the silica and Pd surface to be covered by approximately one statistical monolayer of Ar based on BET surface area measurements. The IFEFFIT package was used for XAS data processing and analysis.[20,21] Energy calibration was performed by aligning all scans with the reference Pd foil prior to further processing. In addition, the parameters used for background subtraction and normalization were kept constant for all scans to ensure that no artifacts were generated from the data normalization procedure. To ensure the differential EXAFS signal produced as a result of subtracting the EXAFS scans before and after Ar adsorption is not due to a slight shift in the zero-point calibration of the *k*-scale, we also reproduced the differential spectrum without alignment of each scan with the reference Pd foil. Additionally, the data normalization procedure is reproducible across multiple EXAFS scans.

Scanning transmission electron microscopy (STEM)

STEM images were acquired at the University of Chicago Research Resources Center facility using a JEOL-ARM 200CF aberration corrected microscope (70 pm spatial resolution and 300 meV energy resolution). STEM imaging for this sample was previously reported.[19] Samples were prepared for analysis by dispersing in isopropyl alcohol, sonicating for 20 min, dropping onto a holey-carbon copper grid, and drying under a heat lamp for 20 min. Images were taken using the high angle annular dark field (HAADF) mode and the Particle2 program was used for counting particle sizes. 90 particles were counted for the particle size distribution.

Computational method

ReaxFF[22] is a classical interatomic interaction force-field that consists of both bonding and non-bonding interactions, which enables the potential to describe both metallic bonding and van der Waals interactions that occur in a system consisting of Pd clusters exposed to a noble gas. To conduct simulations involving metal–metal and metal–noble gas interactions, we combined a recently developed ReaxFF Pd/Pd[23] interaction potential (which was trained against DFT and experimental structural data and formation energies for Pd bulk, surfaces, and clusters) with Ar and He parameter sets.[24] Model Pd_{43} clusters (1 nm diameter) were generated using a hybrid Monte Carlo-molecular dynamics scheme (MC/MD),[23] in which MC steps randomly displace Pd atoms in the cluster according to the usual Metropolis criteria.[25] After every 500 MC trial steps, a 100 ps MD run was conducted to diversify the configuration space explored by the cluster. The temperature of the MC/MD simulation was set to 500 K, which corresponds to the temperature of the experimental system prior to being quenched to 77 K. Hence, the MC/MD simulation yields a set of model clusters in reasonable approximation to those contained in the poly-disperse experimental sample upon exposure to Ar gas, albeit not including the silica support present in the experimental system.

To assess the impact of an Ar gas phase on Pd cluster reconstruction, we conducted molecular dynamics simulations in the NVT ensemble *via* the velocity Verlet method[26] with a 0.25 fs time step. A Berendsen thermostat[27] with a damping constant of 100 fs was used to maintain a temperature of 77 K through the duration of the 1 ns simulations. The model clusters were equilibrated for 1 ns in vacuum before being exposed to 50 gas phase Ar atoms in a 50 $\times$ 50 $\times$ 50 Å periodic simulation cell (yielding an effective pressure of $\sim$0.5 MPa, estimated from the ideal gas law) for an additional 1 ns. Average Pd–Pd bond

distances were determined for each atom from atomic coordinates that were archived at 125 fs intervals throughout the simulation. Additional control simulations were conducted under He to ensure that observed Pd cluster reconstructions can be attributed to the Ar gas phase.

Nearest-neighbor (NN) coordination numbers were calculated using a cutoff radius of 3.5 Å around each atom. The Ar-induced bond length expansion was calculated by taking the difference between the average NN bond length of each atom before and after being exposed to Ar. The data were averaged over the last 125 ps (1000 frames) of each simulation to obtain representative NN bond lengths and coordination numbers.

Results

Adsorption of Ar on Pd/SiO_2 at 77 K

The Pd K-edge EXAFS data for the Pd NCs at 77 K under a He atmosphere (30 mL min^{-1}) are shown in Fig. 1 (referred to as "Clean Pd NCs"). After reduction at 523 K with 3% H_2/He, the sample was purged with pure He prior to cooling to prevent palladium hydride (PdH_x) formation. Based on the Pd–Pd first shell bonding distance, it is clear PdH_x is absent in the sample. The data show only Pd–Pd bonding and there is no indication of low-*Z* scatterers (*e.g.* C, O, or N). The first shell was modeled with a single Pd–Pd scattering path and the fit is shown along with the data in Fig. 1. The results of the fit are shown in Table 1. The clean Pd NCs have a Pd–Pd coordination number and bond length of 7.0 ± 0.2 and 2.700 ± 0.005 Å, respectively. The bond length is contracted with respect to Pd foil, indicating the presence of small Pd NCs, which is in agreement with STEM data. The coordination number is consistent with Pd nanoclusters of about 37 atoms (Pt_{37}).[28,29] A Pd_{37} cluster with the hemispherical (111)-truncated cuboctahedron geometry has a fist shell coordination number of 6.97 and diameter of 1.1 nm. Attempts to fit the EXAFS data past the first coordination shell following established methods[29,30] failed due to the high disorder of the ultra-small Pd NCs. A STEM image for the sample is shown in Fig. 2. The average particle size determined from STEM is 1.0 ± 0.2 nm, which is consistent with the EXAFS results (1.1 nm).

Table 1 Pd K-edge EXAFS first shell fits

Sample	N^a	r (Å)	$\sigma^{2\,b}$ (Å^2)
Pd foil	12	2.731 ± 0.002	0.0058 ± 0.0002
Clean Pd NCs	7.0 ± 0.2	2.700 ± 0.005	0.0088 ± 0.0002
After Ar adsorption	7.2 ± 0.4	2.707 ± 0.008	0.0094 ± 0.0004

[a] Calculation of N was performed using the amplitude reduction factor obtained from the Pd foil (0.86). [b] EXAFS Debye–Waller factor.

After Ar adsorption (5 mL min^{-1} Ar in 30 mL min^{-1} He), the EXAFS data highly resemble the data for the clean Pd NCs. The first shell fit of the data after Ar adsorption provides identical results (within error) to the clean Pd NCs. This analysis strategy, however, is not adequate for detection of changes that may have occurred in Ar atmosphere because only a few surface atoms of Pd particles would have been affected by Ar whereas the XAS signal probes all atoms in the NC. Differential EXAFS (Δ-EXAFS) spectrum obtained after subtracting the two spectra (the one measured in Ar from the other, measured in He) should have much greater sensitivity to the atoms directly affected by Ar because the contributions to the Δ-EXAFS from unaffected ("spectator") atoms will cancel. The Δ-EXAFS signal is shown in Fig. 3. The most striking characteristic of this spectrum is a shift of the phase of the oscillations by *ca.* π/2, clearly visible in Fig. 3. We will show analytically below that the π/2 phase shift in the Δ-EXAFS compared to the total spectrum is consistent with a small change of the Pd–Pd bond length provided that the total coordination number of Pd atoms remains approximately the same. After the adsorption of Ar, the sample was heated to room temperature and purged with flowing He (30 mL min^{-1}) and subsequently cooled to 77 K. Taking the difference of the clean Pd NCs EXAFS spectrum and a spectrum after heating to room temperature shows only noise (see Fig. S2 in the ESI†): therefore, the observed change in the Pd bond length is reversible.

We believe that the Δ-EXAFS signal arises soley due to Ar adsorption, and is not influenced by any impurities present in

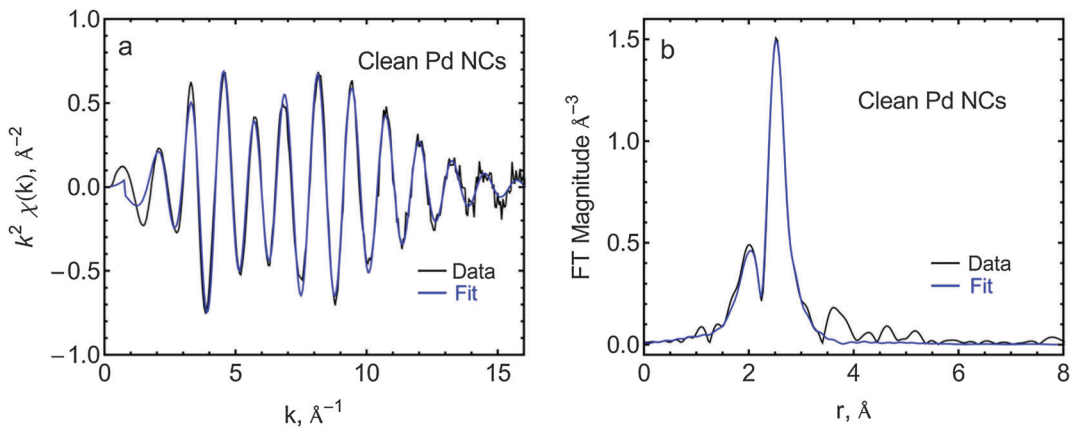

Fig. 1 (a) Edge-step normalized and background-subtracted k^2-weighted $\chi(k)$ EXAFS data and (b) Fourier transform magnitude of k^2-weighted $\chi(k)$ for the clean Pd NCs in He atmosphere at 77 K at the Pd K-edge. The first-shell fit of the data is shown in blue.

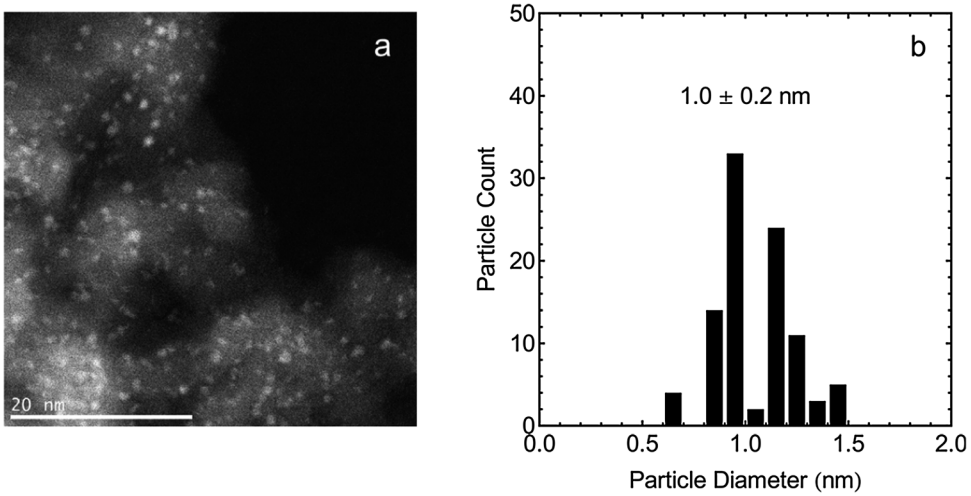

Fig. 2 (a) STEM image of Pd/SiO_2 nanoclusters and (b) particle size distribution of Pd/SiO_2 catalyst. The calculated number average particle diameter is 1.0 ± 0.2 nm.

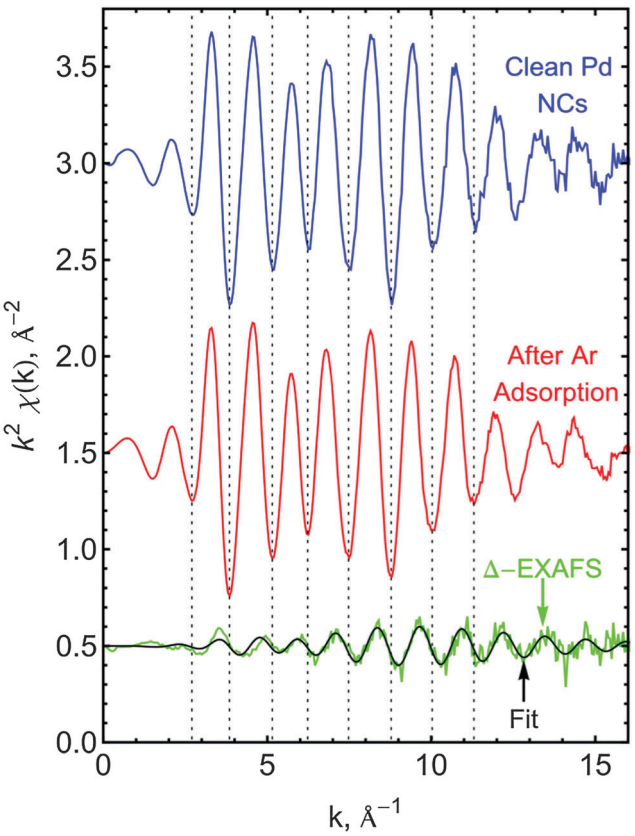

Fig. 3 k^2-weighted $\chi(k)$ EXAFS data for the clean Pd NCs, after Ar adsorption, and the Δ-EXAFS spectrum obtained by subtracting the spectrum after Ar adsorption from the clean Pd NCs spectrum. The fit of the Δ-EXAFS data is shown in black. The dotted lines are a guide to the eye to show the π/2 phase shift of the Δ-EXAFS compared to the original spectrum for Pd NCs. The data are shifted vertically for clarity.

the inert gas streams. Based on the amount of oxygen, nitrogen and water present in either the He or Ar cylinder, the number of surface Pd atoms present in the Pd/SiO_2 catalyst is $\sim 10^4$ greater than the number of impurity molecules introduced to the catalyst over the course of the entire experiment. Additionally, the UHP He contains similar impurities to that of UHP Ar, so if O_2 or H_2O were the primary cause of the observed results we would expect the inert gases to have the same influence both before and after the introduction of Ar and cancel after taking the differential spectrum.

XANES spectra for the clean Pd NCs, the NCs after Ar adsorption, and a reference Pd foil are shown in Fig. S3 in the ESI.† The XANES of the Pd NCs show little difference before and after Ar adsorption, indicative of no change in electronic structure of the Pd atoms.

Below, we describe a general method useful for the analysis of differential EXAFS data of small metal nanoclusters and provide a quantitative assessment of the restructuring of the Pd NCs. The EXAFS signal $\chi(k)$ for modeling the first shell scattering of a NC with two types of bonds, core (i) and surface (i′) (prime refers to surface bonds) is shown below:

$$\chi(k) = \frac{S_0^2 N_i f(k) e^{-\frac{2r_i}{\lambda(k)}} e^{-2k^2\sigma_i^2}}{kr_i^2} \sin(2kr_i + \delta(k)) + \frac{S_0^2 N_{i'} f(k) e^{-\frac{2r_{i'}}{\lambda(k)}} e^{-2k^2\sigma_{i'}^2}}{kr_{i'}^2} \sin(2kr_{i'} + \delta(k)) \quad (1)$$

where k is the photoelectron wave number, S_0^2 is the passive electron reduction factor, $f(k)$ and $\delta(k)$ are the photoelectron scattering-path amplitude and phase, respectively, N is the coordination number, r is the interatomic distance, σ^2 is the mean-square deviation in r, and $\lambda(k)$ is the photoelectron mean free path. Correspondingly, the EXAFS equation for the "Clean Pd NCs" sample, χ_{Clean}, is:

$$\chi_{Clean}(k) = \frac{S_0^2 N_1 f(k) e^{-\frac{2r_1}{\lambda(k)}} e^{-2k^2\sigma_1^2}}{kr_1^2} \sin(2kr_1 + \delta(k)) + \frac{S_0^2 N_{1'} f(k) e^{-\frac{2r_{1'}}{\lambda(k)}} e^{-2k^2\sigma_{1'}^2}}{kr_{1'}^2} \sin(2kr_{1'} + \delta(k)) \quad (2)$$

The EXAFS equation for the "After Ar adsorption" sample, χ_{After}, is:

$$\chi_{After}(k) = \frac{S_0^2 N_2 f(k) e^{-\frac{2r_2}{\lambda(k)}} e^{-2k^2\sigma_2^2}}{kr_2^2} \sin(2kr_2 + \delta(k)) + \frac{S_0^2 N_{2'} f(k) e^{-\frac{2r_{2'}}{\lambda(k)}} e^{-2k^2\sigma_{2'}^2}}{kr_{2'}^2} \sin(2kr_{2'} + \delta(k)) \quad (3)$$

Since the interior atoms are unchanged during the adsorption of Ar, $N_1 = N_2$, $r_1 = r_2$, and ${\sigma_1}^2 = {\sigma_2}^2$. In addition, ${S_0}^2$, $f(k)$, and $\lambda(k)$ will be identical in all terms since they all refer to a Pd–Pd single scattering path. The number of surface atoms, $N_{1'}$ or $N_{2'}$ will also remain unchanged and this will be referred to as N_s. If eqn (3) is subtracted from eqn (2), the following expression is derived for Δ-EXAFS ($\chi_{Clean} - \chi_{After}$):

$$\Delta\text{-EXAFS} = \frac{S_0^2 N_s f(k) e^{-\frac{2r_{1'}}{\lambda(k)}} e^{-2k^2\sigma_{1'}^2}}{kr_{1'}^2} \sin(2kr_{1'} + \delta(k)) - \frac{S_0^2 N_s f(k) e^{-\frac{2(r_{1'}+\Delta r)}{\lambda(k)}} e^{-2k^2\sigma_{2'}^2}}{k(r_{1'} + \Delta r)^2} \times \sin(2k(r_{1'} + \Delta r) + \delta(k)) \quad (4)$$

where $r_{2'}$ is expressed as $r_{1'} + \Delta r$. We note that eqn (4), in the approximation that the bond length disorder did not change between the two states and that $\Delta r \ll r$, eqn (4) reduces to a simple ansatz (a complete derivation of eqn (5) is provided in the ESI†):

$$\Delta\text{-EXAFS} \approx \frac{S_0^2 N_s f(k) e^{-\frac{2r_{1'}}{\lambda(k)}} e^{-2k^2\sigma_{1'}^2}}{kr_{1'}^2} (2k\Delta r) \sin\left(2kr_{1'} + \delta(k) + \frac{\pi}{2}\right) \quad (5)$$

Eqn (5) shows that for small variations in the bond length, Δr, the differential EXAFS spectrum will display a π/2 phase shift compared to the original EXAFS spectrum (χ_{Clean}). This validates our conclusions based on visual examination of the Δ-EXAFS (Fig. 3) which also shows the π/2 phase shift compared to the spectrum measured in He or Ar atmospheres. We note that eqn (5) is equivalent to that used for analysis of differential signal in magnetostriction experiment by modulation excitation method.[18]

The differential spectrum can be modeled by implementing eqn (4) into a suitable data analysis program. In this work it was accomplished by using FEFF models for each spectrum and fitting the difference between the two modeled signals to the experimental data. The total number of Pd–Pd bonds affected by Ar adsorption, $n_{Pd-Pd,aff}$, can be estimated directly from the measured N_s, the coordination number of Pd–Pd atoms in the differential spectrum, and the total number of atoms in a representative particle (n) as follows:

$$N_s = \frac{2n_{Pd-Pd,aff}}{n} \quad (6)$$

We note that the denominator is the total number of atoms per particle, not the total number of affected atoms, which would make it analogous to a conventional expression for coordination number[31] because the differential signal was obtained by subtracting the edge-step normalized EXAFS spectrum. Edge step normalization is the procedure that relates the total EXAFS signal from all absorbing atoms in the sample to that corresponding to an "an equivalent absorber", hence, the total number of atoms is used in the denominator of eqn (6).

Table 2 Fit parameters obtained from the differential data using eqn (4)

Parameter	Value	Allowed to vary?
N_S	0.46 ± 0.07	Yes
$r_{1'}$	2.700 ± 0.005 Å	No[a]
${\sigma_{1'}}^2$	0.0088 ± 0.0002 Å^2	No[a]
Δr	0.104 ± 0.005 Å	Yes
${\sigma_{2'}}^2$	0.0045 ± 0.0009 Å^2	Yes
$n_{Pd-Pd,aff}$	9 ± 2	[b]

[a] Obtained from fit of clean Pd NCs. [b] Determined after the fit using eqn (6), where n = 37.

The terms $r_{1'}$ and ${\sigma_{1'}}^2$ were obtained from the fit of the "Clean Pd NCs" (Fig. 1 and Table 1) under the approximation the surface atoms have a bond length and EXAFS Debye–Waller factor equivalent to the bulk value of the Pd NCs (*i.e.* $r_1 = r_{1'}$ and ${\sigma_1}^2 = {\sigma_{1'}}^2$). However, in other cases, higher data quality may allow for the determination of $r_{1'}$ and ${\sigma_{1'}}^2$ directly from the differential data.

The results of fitting the Δ-EXAFS with eqn (4) are presented in Table 2, and the Fourier transform magnitude EXAFS for the data and the fit are presented in Fig. 4. The number of Pd–Pd bonds that changed during the Ar-induced restructuring is 9 ± 2. These bonds expanded by Δr = 0.104 ± 0.005 Å. In addition, the disorder of these bonds decreased since the EXAFS Debye–Waller factor decreased from 0.0088 ± 0.0002 Å^2 to 0.0045 ± 0.0009 Å^2. Thus, the EXAFS analysis shows that 9 ± 2 NN Pd–Pd bonds expand as a result of introducing Ar at 77 K. This is compared to the total number of NN Pd–Pd bonds in a 37-atom Pd cluster of 129.

EXAFS analysis by fitting method often depends on the model used, and comparing several models is necessary to avoid possible

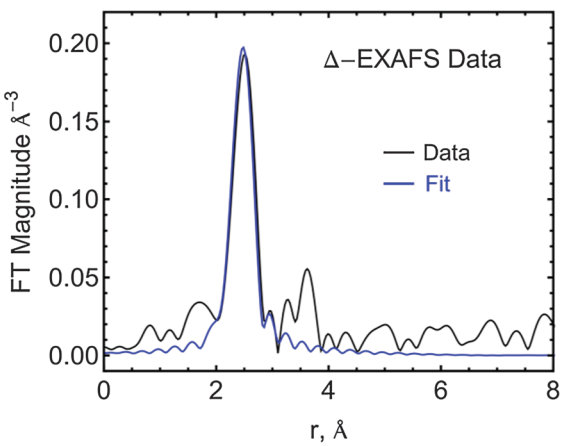

Fig. 4 Fourier transform magnitude of k^2-weighted $\chi(k)$ for the Δ-EXAFS spectrum (black) and the fit of the data (blue) using the model in eqn (4).

misinterpretation of the data. We have compared two additional models that are described below. The first model was a Pd–Ar single-scattering model that assumes that the differential signal could arise from Pd–Ar scattering only. Attempts to fit the Δ-EXAFS signal with the Pd–Ar scattering model (Table S1 of the ESI†) results in an unrealistic fit parameter for the energy shift and a poor-quality fit to the data. Therefore, we dismiss the possibility that the differential signal arises from Pd–Ar contributions. The second model was a direct fit of the differential data with Pd–Pd scattering (Table S2 of the ESI†). This model would only be appropriate if the number of Pd–Pd bonds changed, such that the amplitude of the differential data represents additional Pd–Pd bonds that arose during the adsorption of Ar (or Pd–Pd bonds that were removed during the adsorption). Fitting the differential data with this model results in a good fit to the data, and the Pd–Pd bond length expansion was comparable to what was found in the present differential model EXAFS model. However, this model assumes the overall Pd–Pd coordination number changed during Ar adsorption. On the other hand, the differential EXAFS model described in eqn (4) shows that the differential EXAFS signal arises from a change in bond length only, with no change in the overall Pd–Pd coordination number. Thus, using EXAFS alone, it is impossible to differentiate between the two aforementioned models. We show through the atomistic modeling described below that we are able to use theory to break the degeneracy of the two competing EXAFS models.

Atomistic modeling of Ar-induced restructuring

To support our experimental observation of Ar-induced surface restructuring of Pd atoms and to differentiate between the proposed EXAFS models, we conducted a series of ReaxFF-MD simulations in which model Pd clusters were exposed to both vacuum and an Ar gas phase (*i.e.* 50 Ar atoms in the periodic cell) at 77 K. In each simulation, the average Pd–Pd bond distance was assessed from the atomic coordinates of the system, thus allowing changes in average Pd–Pd bond distance after the introduction of Ar atoms to be determined. Fig. 5 depicts the initial and final system geometries in an MD simulation where a 1 nm Pd cluster was exposed to Ar. As seen in the figure, Ar interacts weakly with the cluster, forming a physisorbed layer of Ar atoms on the surface of the cluster. The calculated adsorption energy for an isolated Ar atom on Pd is 1–2 kcal mol^{-1}, which is dependent on the adsorption configuration.

To assure modeling results were not biased by the initial selection of cluster geometry, we employed a hybrid MC/MD simulation method to generate a set of model Pd clusters. The MC/MD simulation was conducted at 500 K, which corresponds to the experimental annealing temperature the Pd clusters were exposed to before being quenched to 77 K. This results in an ensemble of cluster geometries that are representative of those present in the experimental sample, where the energy differences between clusters arise due to thermal fluctuations in the system, as shown in Fig. 6. The model clusters do not include the SiO_2 support used experimentally, and therefore we neglect any effect the support could have on initial Pd nanocluster structure or the restructuring process. The relative impact of this simplification is further addressed in the discussion section.

We selected 50 clusters (using a random number generator) from the 500 K MC/MD sample set to serve as starting geometries for MD simulations at 77 K. The selected clusters correspond to the green and red data points in Fig. 6. During each 77 K MD simulation, average Pd–Pd bond distances were determined by calculating the Pd–Pd radial pair distribution, $g(r)$, over the last 250 ps of the 1 ns MD simulations. As shown in Fig. 7 for a single cluster geometry, each simulation initially allows the Pd cluster to equilibrate at 77 K for 1 ns in vacuum before exposure to Ar (or He/vacuum in the case of control simulations). As seen in the figure, the simulation yields no change in Pd–Pd bond distance after exposure to vacuum or He, whereas cluster restructuring with a 0.003 Å Pd–Pd expansion occurs under Ar. The radial distribution function in Fig. 7(d), in comparison to those for control simulations in Fig. 7(a–c), demonstrates a clear restructuring of the cluster, where the shoulder appearing at $r = \sim 2.60$ Å in the control simulations shifts to $r = \sim 2.75$ Å (indicated by black arrows in the figure). This suggests the average Pd–Pd bond expansion can be attributed to a large increase in a few Pd–Pd bonds involving one or two atoms, as opposed to a small increase in all Pd–Pd bonds throughout the cluster. This is further depicted in Fig. 8,

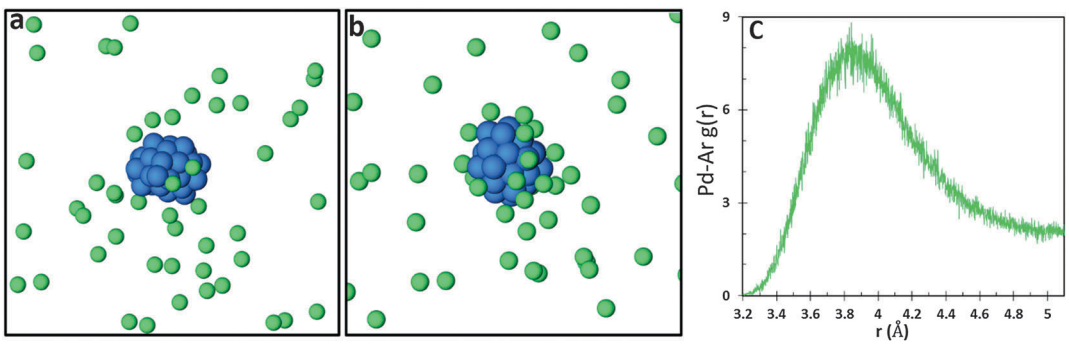

Fig. 5 (a) Initial and (b) final system geometry in a 1 ns MD-NVT simulation at 77 K. (c) Pd–Ar radial pair distribution function, $g(r)$, demonstrating an Ar physisorption well centered near $r = \sim 3.9$ Å from the cluster surface.

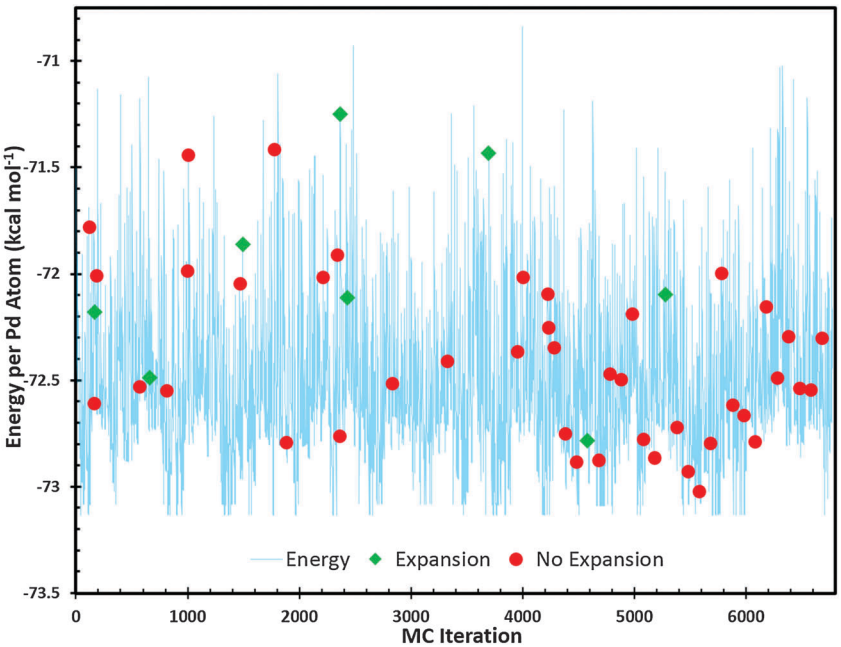

Fig. 6 Energy of Pd clusters generated from a hybrid MC/MD simulation at 500 K. The green and red data points indicate clusters that were selected for separate MD simulations to assess Pd–Pd expansion upon exposure to Ar. The color coding of these dots classifies the results obtained from the subsequent 77 K MD runs in the presence of Ar. Green diamonds indicate that an average Pd–Pd expansion >0.001 Å was observed and red dots indicate that there was no change >0.001 Å.

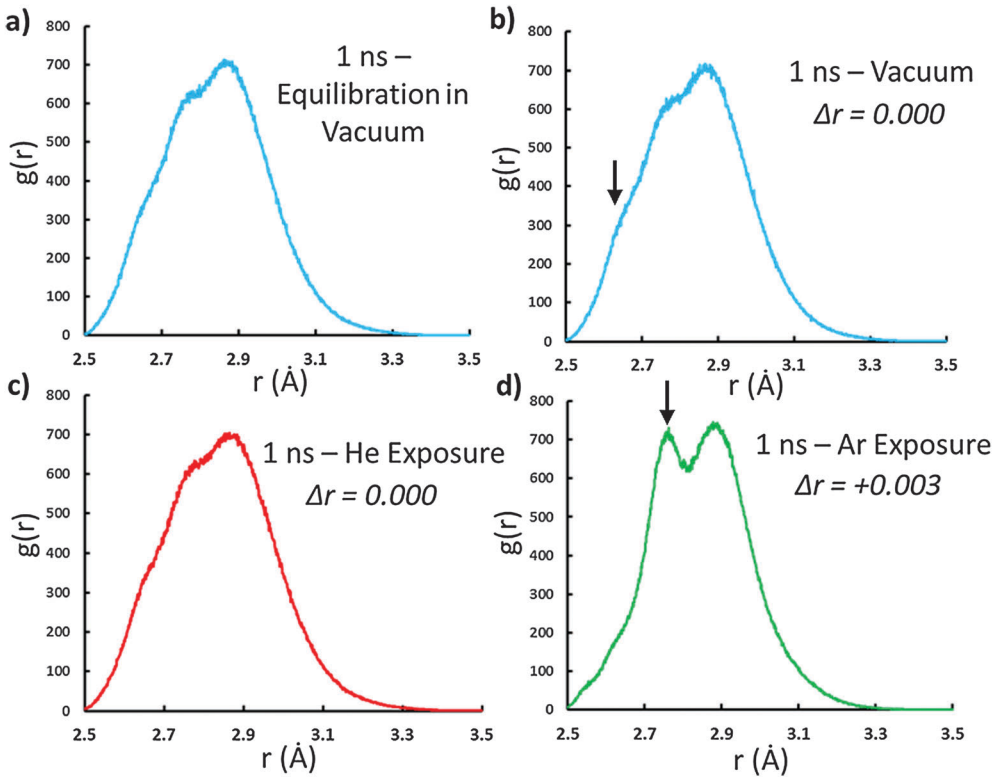

Fig. 7 Pd–Pd radial distribution function, $g(r)$, reflecting the average NN Pd–Pd bond distances during a 1 ns MD simulation at 77 K. (a) The Pd cluster was first allowed to equilibrate in vacuum for 1 ns, and was then exposed to (b) vacuum, (c) He gas, or (d) Ar gas for an additional 1 ns. Arrows indicate the peak shift attributed to the average Pd–Pd bond expansion of an under-coordinated surface atom.

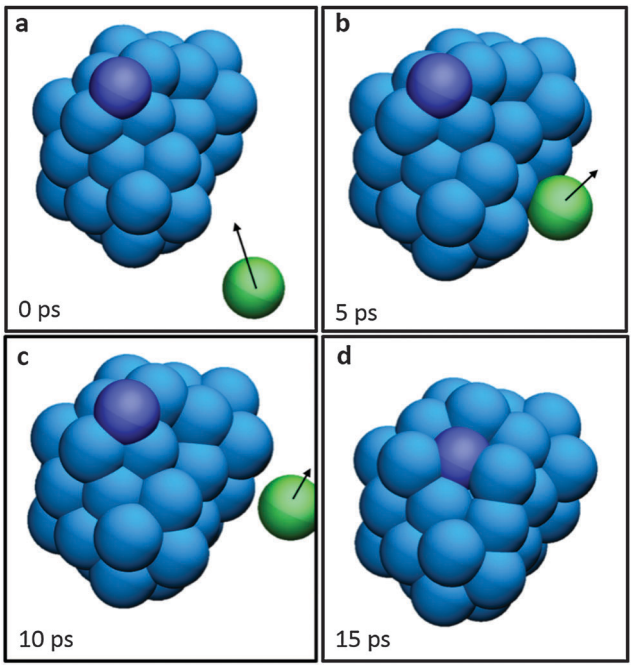

Fig. 8 A 15 ps MD trajectory window demonstrating an Ar (green) collision with a Pd cluster (blue) inducing the restructuring of an under-coordinated Pd surface atom (purple). Only the Ar atom interacting with the Pd cluster is shown, all others are omitted for clarity.

which shows snapshots from the 15 ps MD-trajectory window in which the surface restructuring occurs. The restructuring occurs immediately after the Pd cluster interacts with an incoming Ar atom, suggesting that the momentum transfer from the Ar atom to the cluster induces the surface reconstruction. This reconstruction does not occur in the absence of the Ar gas phase. An animated video of this 15 ps trajectory demonstrating surface reconstruction is provided in the ESI,† along with a 250 ps video of the cluster in vacuum showing no reconstruction.

A similar analysis was conducted for all 50 model clusters, where 8 clusters demonstrated an average Pd–Pd bond length expansion greater than 0.001 Å upon exposure to Ar and the remaining 42 exhibited no change greater than 0.001 Å, indicated by green diamonds and red dots, respectively, in Fig. 6. The expansion of Pd–Pd bond lengths was further quantified by assessing the average Pd–Pd bond length change for a single Pd atom as a function of its average coordination number under vacuum conditions. This is shown in Fig. 9, where we have plotted average bond length expansion against coordination number in vacuum averaged over all 50 clusters investigated. Fig. 9(a) contains data from clusters that exhibited an expansion, while Fig. 9(b) contains data from clusters that did not exhibit expansion. This analysis reveals that only under-coordinated Pd atoms with low nearest-neighbor coordination numbers (*i.e.*, 3–5) are affected by the adsorption of Ar, with a typical bond length expansion of *ca.* 0.05 to 0.1 Å. Fig. 9(b) demonstrates some under-coordinated atoms are not affected by the Ar gas phase, indicating that some under-coordinated atoms are more stable than others. Observed coordination numbers greater than 12 reflect that these clusters have a disordered, non-crystalline lattice structure, which is expected for platinum-group-metals in this size range.[32]

Since Ar induces restructuring of under-coordinated surface atoms, it is likely that these atoms are kinetically trapped in metastable positions during the quench to 77 K, and that a transfer of kinetic energy from an Ar gas phase atom provides the additional energy required to allow relaxation of the metastable Pd atom to a more favorable site with higher average coordination and longer average Pd–Pd bonds. Not all under-coordinated sites are affected by Ar, which could be the result of short simulation timescales, where a sufficient Pd–Ar interaction simply never occurred in the simulation timeframe. Also, some under-coordinated sites may be more stable than others, indicating that Ar can only induce the restructuring of

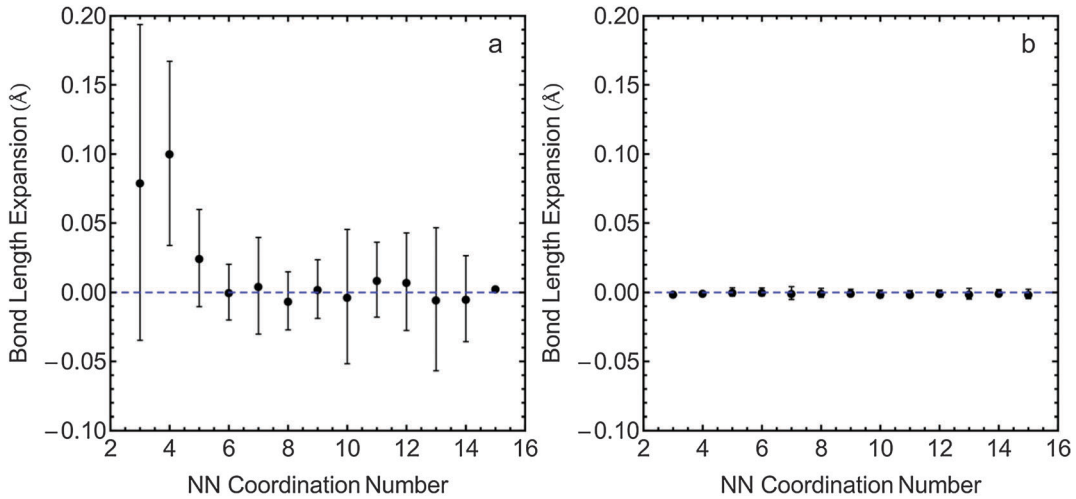

Fig. 9 Bond length expansion (relative to the clusters in vacuum) plotted *versus* first shell coordination number for all of the atoms in each of the Pd clusters that (a) exhibited expansion and (b) did not exhibit expansion after exposure to Ar at 77 K. Error bars indicate the standard deviation in bond length of the ensemble of atoms from all of the clusters.

sufficiently unstable Pd atoms. A ReaxFF nudged-elastic-band (NEB) barrier calculation (provided in Fig. S4 of the ESI†) yielded a barrier of 11.4 kcal mol^{-1} for the reconstruction shown in Fig. 8, which is sufficiently high to suggest that this structure would be kinetically stable at 77 K under vacuum. Together, these simulations demonstrate Ar may drive surface reconstructions of under-coordinated atoms, thus leading to an increased Pd–Pd bond length of surface Pd atoms, in agreement with the experimental observations above.

Discussion

Analysis of the differential EXAFS data using the model in eqn (4) shows that Ar adsorption on Pd/SiO_2 at 77 K induces small changes in the Pd–Pd coordination environment, which can be attributed to the expansion in the bond length of surface Pd atoms. However, this model was created under the presumption that the overall Pd–Pd coordination number remained unchanged during Ar adsorption, and the correctness of such an approximation can be verified by examining simulated clusters before and after Ar adsorption. We calculated the average Pd–Pd coordination number of the clusters shown in Fig. 9(a) before and after Ar adsorption. The results are presented in Table 3. In each of the 8 simulations in which Ar caused restructuring, under-coordinated Pd atoms formed new Pd–Pd bonds, which is concomitant with expansion in their bond length. The number of Pd–Pd bonds formed varied, as this is dependent on the starting structure. Meanwhile, a similar number of Pd–Pd bonds were broken such that the average change in Pd–Pd coordination number was ~ 0. Therefore, the atomistic simulations are in agreement with the proposed differential EXAFS model in eqn (4) and the experimental results shown in Table 2.

Restructuring without an overall coordination number change requires strongly disordered nanoclusters because restructuring of a faceted particle will always lead to either an increase or decrease in coordination number if the total number of atoms in the particle remains the same. McKenna and Shluger showed that faceted Au nanoparticles restructure under CO adsorption, leading to an increase in coordination number.[33] Thus, for our theoretical models to be compatible with those real clusters used in our experiments, it is advantageous to model strongly disordered Pd/SiO_2 NCs rather than faceted, crystalline, structures. Experimentally it has been demonstrated that alumina- and carbon-supported Pt clusters are predominantly non-crystalline in the size range less than 1–1.5 nm.[32]

The high effective pressure of Ar and omission of SiO_2-supported Pd NCs from the theoretical portion of this study are limitations in obtaining quantitative results of the restructuring. We expect that introduction of the SiO_2 support might result in a different distribution in Pd particle shapes and the time scale for energy transfer from Ar to Pd could be impacted by dissipation into the support. However, the overall mechanism for restructuring is likely independent of support, since the exposed Pd atoms in low coordination environments present on the Pd particle exterior, which participate in the observed restructuring, would likely not be adjacent to the support. Furthermore, the large difference in masses between Pd and SiO_2 suggest minimal vibrational coupling, and therefore we could expect that dissipation of kinetic energy passed from Ar to Pd may remain in Pd related modes on the time scale observed in the simulations. Thus, atomistic modeling qualitatively supports the hypothesis that under-coordinated surface atoms are those affected and helps us gain an atomistic level understanding of the process.

Other examples of Ar-induced restructuring include the work of Pellenq *et al.* who measured the neutron diffraction of ^{40}Ar adsorption in silicate-1 zeolite and showed that a step in the Ar isotherm coincides with a change in the neutron diffraction pattern.[34] Using grand canonical Monte Carlo simulations (GCMC), the authors concluded the change in diffraction pattern can be attributed to a rearrangement of the adsorbed phase. This conclusion has been further substantiated by García-Pérez *et al.*, who showed through GCMC simulations that a flexible host structure is likely responsible for the stepped Ar isotherm at 77 K for a MFI zeolite.[35] More recently, Mallon *et al.* surmised that the hysteresis of the Ar 87 K adsorption isotherm of silicate-1 is a result of an orthorhombic–monoclinic symmetry shift.[36] On the other hand, Ar ion bombardment at low energy (*ca.* 15 eV) has been shown to heal defects of carbon nanotubes.[37]

We have performed steady-state experiments where only a single factor was changed at a time. Fig. S5 (ESI†) shows two differential EXAFS spectra: the differential spectrum that we presented in the manuscript and the spectrum obtained by subtracting the spectrum after Ar was replaced by He from the original spectrum collected in He. Both differential spectra were measured at the same temperature (77 K). The presence of EXAFS-like oscillations of the first spectrum when Ar was present is in obvious contrast to the second spectrum that is dominated by statistical noise. In our view, this is sufficient evidence that the changes we have described are due to the influence of Ar. The second differential spectrum also characterizes temperature stability as excellent. If the sample temperature was not identical before and after Ar was replaced by He, the differential signal would have shown (and it does not) systematic features, due to the difference in the thermal factors.

Table 3 Coordination environment changes of Pd clusters as a result of Ar adsorption

Simulation[a]	# of Pd–Pd bonds formed[b]	# of Pd–Pd bonds broken[c]	Δ avg NN CN[d]
1	7.2	−9.6	−0.06
2	9.0	−9.8	−0.02
3	3.2	−1.3	0.04
4	5.1	−3.0	0.05
5	5.7	−1.0	0.11
6	4.5	−1.1	0.08
7	3.0	−5.0	−0.05
8	2.7	−7.1	−0.10
Average[e]	5.1	−4.7	0.01

[a] Simulations in which Ar caused restructuring. [b] Number of Pd–Pd bonds formed during Ar adsorption. [c] Number of Pd–Pd bonds that were broken during Ar adsorption. [d] Average nearest-neighbor coordination number after Ar adsorption minus the average nearest-neighbor coordination number under vacuum. [e] Average over simulations 1–8.

The EXAFS differential data analysis method we detail in this paper is applicable to other systems where only a small fraction of surface species (active species) respond to the external stimulation (*e.g.* gas, pH, electric potential, temperature, *etc.*) while the majority of the atoms (spectators) are unaffected. In this study, we are able to measure a change in coordination environment of only 7% of the total number of Pd atoms, which highlights the sensitivity of the combined measurement and analysis scheme.

Conclusions

Differential extended X-ray absorption fine structure (Δ-EXAFS) and atomistic molecular dynamic simulations have been used to detect under-coordinated surface Pd atoms of SiO_2-supported nanoclusters. The increased sensitivity of Δ-EXAFS allows for detection of small changes in the coordination environment of surface Pd atoms that would otherwise be undetected with conventional XAS techniques. Differentiating between possible models, a common problem associated with EXAFS analysis, was accomplished through analysis of the simulation results. Further theoretical modeling of supported clusters might provide quantitative comparison between experiment and theory.

Using an inert gas such as Ar to probe surface atoms may be advantageous over conventional surface probe molecules such as CO, NO, and H_2 because it physically adsorbs without specificity, different from the highly selective binding associated with chemical adsorption. In this regard, inert gas adsorption might prove to be a general method for determining surface composition of multimetallic catalysts. We also note the possibility of using Δ-EXAFS at the Ar K-edge or Kr K-edge to probe metal surfaces from the perspective of the inert gas.

Acknowledgements

Use of the Advanced Photon Source was supported by the U.S. Department of Energy, Office of Science, Office of Basic Energy Sciences, under Contract No. DE-AC02-06CH11357. MRCAT operations are supported by the Department of Energy and the MRCAT member institutions. C. S. S. acknowledges the National Science Foundation under Grant No. DGE1255832. T. P. S., A. C. T. v. D., and M. J. J. acknowledge funding from the National Science Foundation under Grant No. CBET-1032979. Any opinions, findings, and conclusions or recommendations expressed in this material are those of the author(s) and do not necessarily reflect the views of the National Science Foundation. C. S. S., R. M. R., and A. I. F. acknowledge funding from the Department of Energy, Office of Basic Energy Sciences, Chemical Sciences, Geosciences, and Biosciences Division, Catalysis Sciences Program under grant numbers DE-FG02-12ER16364 (to R. M. R.) and DE-FG02-03ER15476 (to A. I. F.). R. M. R. acknowledges support from the Air Force Office of Scientific Research (AFOSR, No. FA9550-12-1-0204). The authors thank Randall J. Meyer, David Childers, and Jeffrey T. Miller for providing the Pd/SiO_2 sample and STEM images.

References

1 J. Rao, *ACS Nano*, 2008, **2**, 1984–1986.
2 S. I. Sanchez, L. D. Menard, A. Bram, J. H. Kang, M. W. Small, R. G. Nuzzo and A. I. Frenkel, *J. Am. Chem. Soc.*, 2009, **131**, 7040–7054.
3 D. Pacifici, H. J. Lezec and H. A. Atwater, *Nat. Photonics*, 2007, **1**, 402–406.
4 D. Alloyeau, C. Ricolleau, C. Mottet, T. Oikawa, C. Langlois, Y. Le Bouar, N. Braidy and A. Loiseau, *Nat. Mater.*, 2009, **8**, 940–946.
5 A. Sundaresan, R. Bhargavi, N. Rangarajan, U. Siddesh and C. N. R. Rao, *Phys. Rev. B: Condens. Matter Mater. Phys.*, 2006, **74**, 161306.
6 J. K. Norskov, T. Bligaard, J. Rossmeisl and C. H. Christensen, *Nat. Chem.*, 2009, **1**, 37–46.
7 M. S. Chen and D. W. Goodman, *Science*, 2004, **306**, 252–255.
8 P. L. Hansen, J. B. Wagner, S. Helveg, J. R. Rostrup-Nielsen, B. S. Clausen and H. Topsøe, *Science*, 2002, **295**, 2053–2055.
9 H. J. Freund, *Chem. – Eur. J.*, 2010, **16**, 9384–9397.
10 A. R. Tao, S. Habas and P. Yang, *Small*, 2008, **4**, 310–325.
11 T. Wu, D. J. Childers, C. Gomez, A. M. Karim, N. M. Schweitzer, A. J. Kropf, H. Wang, T. B. Bolin, Y. Hu, L. Kovarik, R. J. Meyer and J. T. Miller, *ACS Catal.*, 2012, **2**, 2433–2443.
12 A. Eyssler, E. Kleymenov, A. Kupferschmid, M. Nachtegaal, M. S. Kumar, P. Hug, A. Weidenkaff and D. Ferri, *J. Phys. Chem. C*, 2010, **115**, 1231–1239.
13 D. Ferri, M. S. Kumar, R. Wirz, A. Eyssler, O. Korsak, P. Hug, A. Weidenkaff and M. A. Newton, *Phys. Chem. Chem. Phys.*, 2010, **12**, 5634–5646.
14 D. Ferri, M. Newton and M. Nachtegaal, *Top. Catal.*, 2011, **54**, 1070–1078.
15 D. Ferri, M. A. Newton, M. Di Michiel, S. Yoon, G. L. Chiarello, V. Marchionni, S. K. Matam, M. H. Aguirre, A. Weidenkaff, F. Wen and J. Gieshoff, *Phys. Chem. Chem. Phys.*, 2013, **15**, 8629–8639.
16 C. F. J. König, T. J. Schildhauer and M. Nachtegaal, *J. Catal.*, 2013, **305**, 92–100.
17 C. F. J. König, J. A. van Bokhoven, T. J. Schildhauer and M. Nachtegaal, *J. Phys. Chem. C*, 2012, **116**, 19857–19866.
18 R. F. Pettifer, O. Mathon, S. Pascarelli, M. D. Cooke and M. R. J. Gibbs, *Nature*, 2005, **435**, 78–81.
19 D. Childers, A. Saha, N. Schweitzer, R. M. Rioux, J. T. Miller and R. J. Meyer, *ACS Catal.*, 2013, **3**, 2487–2496.
20 B. Ravel and M. Newville, *J. Synchrotron Radiat.*, 2005, **12**, 537–541.
21 M. Newville, *J. Synchrotron Radiat.*, 2001, **8**, 322–324.
22 A. C. T. van Duin, S. Dasgupta, F. Lorant and W. A. Goddard III, *J. Phys. Chem. A*, 2001, **105**, 9396–9409.
23 T. P. Senftle, R. J. Meyer, M. J. Janik and A. C. T. van Duin, *J. Chem. Phys.*, 2013, **139**, 044109–044115.
24 A. M. Kamat, A. C. T. van Duin and A. Yakovlev, *J. Phys. Chem. A*, 2010, **114**, 12561–12572.
25 N. Metropolis, A. W. Rosenbluth, M. N. Rosenbluth, A. H. Teller and E. Teller, *J. Chem. Phys.*, 1953, **21**, 1087–1092.

26 L. Verlet, *Phys. Rev.*, 1967, **159**, 98–103.
27 H. J. C. Berendsen, J. P. M. Postma, W. F. v. Gunsteren, A. DiNola and J. R. Haak, *J. Chem. Phys.*, 1984, **81**, 3684–3690.
28 A. M. Beale and B. M. Weckhuysen, *Phys. Chem. Chem. Phys.*, 2010, **12**, 5562–5574.
29 A. I. Frenkel, C. W. Hills and R. G. Nuzzo, *J. Phys. Chem. B*, 2001, **105**, 12689–12703.
30 A. Frenkel, *J. Synchrotron Radiat.*, 1999, **6**, 293–295.
31 A. I. Frenkel, *Chem. Soc. Rev.*, 2012, **41**, 8163–8178.
32 L. Li, L.-L. Wang, D. D. Johnson, Z. Zhang, S. I. Sanchez, J. H. Kang, R. G. Nuzzo, Q. Wang, A. I. Frenkel, J. Li, J. Ciston, E. A. Stach and J. C. Yang, *J. Am. Chem. Soc.*, 2013, **135**, 13062–13072.
33 K. P. McKenna and A. L. Shluger, *J. Phys. Chem. C*, 2007, **111**, 18848–18852.
34 R. J. M. Pellenq and D. Nicholson, *Langmuir*, 1995, **11**, 1626–1635.
35 E. García-Pérez, J. B. Parra, C. O. Ania, D. Dubbeldam, T. J. H. Vlugt, J. M. Castillo, P. J. Merkling and S. Calero, *J. Phys. Chem. C*, 2008, **112**, 9976–9979.
36 E. E. Mallon, M. Y. Jeon, M. Navarro, A. Bhan and M. Tsapatsis, *Langmuir*, 2013, **29**, 6546–6555.
37 E. C. Neyts, K. Ostrikov, Z. J. Han, S. Kumar, A. C. T. van Duin and A. Bogaerts, *Phys. Rev. Lett.*, 2013, **110**, 065501.

